Ionics (2019) 25:747–761
https://doi.org/10.1007/s11581-018-2629-9

ORIGINAL PAPER

Incident photon-to-current efficiency of thermally treated SWCNTs-based nanocomposite for dye-sensitized solar cell

Savisha Mahalingam[1] · Huda Abdullah[2] · Nowshad Amin[2] · Abreeza Manap[3]

Received: 24 January 2018 / Revised: 16 May 2018 / Accepted: 11 June 2018 / Published online: 23 June 2018

Abstract

This study focuses on incident photon-to-current efficiency (IPCE) performance of In_2O_3-SWCNTs for dye-sensitized solar cell (DSSC) application. The thin films were prepared by sol-gel method using spin-coating technique annealed at 400, 450, 500, 550, and 600 °C. Morphology transition of In_2O_3 from spherical to cubic and then octahedral structure occurred as the annealing temperature rises. The photoanode annealed at 450 °C (cubic structure) provides a stable phase of cubic structure with large surface area and optimum thickness for effective dye adsorption. However, the IPCE value does not solely depends on the dye adsorption of photoanodes (light harvesting efficiency (LHE)) but the electron injection efficiency (η_{inj}) and the collection efficiency (η_{coll}). Smaller energy bandgap of photoanodes favors the injected electrons with higher driving force to the conduction band (CB) of the photoanode, which in turn increases the η_{inj} from the LUMO of dye to the In_2O_3-SWCNTs CB. Besides that, the absence of single-walled carbon nanotubes (SWCNTs) above 500 °C caused the energy bandgap to increase and leads to lower driving force of injected electrons. In addition, SWCNTs are capable of absorbing visible light faster than other materials. Therefore, the cubic structure-based photoanode (450 °C) exhibited better electron transport with larger driving force on injected electron (η_{inj}) that decreased the electron recombination rate and increased electron lifetime and subsequently obtained larger charge collection efficiency (η_{coll}) of almost 99%. Consequently, the IPCE performance of DSSC was enhanced.

Keywords Dye-sensitized solar cell · In_2O_3 · Single-walled carbon nanotubes · Thermal stability · IPCE

Introduction

Dye-sensitized solar cell (DSSC) converts the clean solar energy into electrical energy by promoting sustainable energy development. DSSC was first introduced by O'Regan and Grätzel in 1991 with low-cost fabrication and simple manufacturing technique with greater performance [1]. As a result, they are more preferable than silicon solar cells. The current solar power conversion efficiency is nearing 15% by using TiO_2 material as photoanode [2]. However, research on alternative photoanodes is still going on for a promising DSSC. The common photoanodes widely studied are ZnO [3, 4], SnO_2 [5, 6], In_2O_3 [7–9], and $SrRuO_3$ [10].

In_2O_3-based DSSC gives longer electron lifetime and slower electron recombination rate than that of TiO_2 [11]. In_2O_3 also provides higher stability observed by the change in light and dark current density-voltage photoelectrochemical performance [11]. However, In_2O_3-based DSSC exhibits low efficiency due to inefficient electron mobility in the cell [12]. As a solution to enhance the electron transport in the photoanode, carbon nanotubes (CNTs) are introduced in solar cells [13–16]. CNT nanocomposites were also used in other applications such as in wireless power transfer, lithium-ion storage, supercapacitors, and many more [17–22].

Generally, CNTs are added as stabilizers in the counter electrode of DSSC to increase the catalytic activity of the cell [23]. In this research, we added CNTs in the photoanode in order to increase the electrical conductivity and performance of DSSC. Acid treatment process on pristine CNTs is an

✉ Savisha Mahalingam
savisha333@yahoo.com.my

1 Institute of Sustainable Energy (ISE), Universiti Tenaga Nasional, Jalan IKRAM-UNITEN, 43000 Kajang, Selangor, Malaysia

2 Department of Electrical, Electronic and System Engineering, Faculty of Engineering and Built Environment, Universiti Kebangsaan Malaysia, 43600 Bangi, Selangor, Malaysia

3 Department of Mechanical Engineering, College of Engineering, Universiti Tenaga Nasional, Jalan IKRAM-UNITEN, 43000 Kajang, Selangor, Malaysia

efficient method to boost the electronic, mechanical, thermal, and adsorption properties [24, 25]. However, In_2O_3-CNTs-based photoanode nanocomposite for DSSC suffers from high-temperature thermal stability.

There are several reasons that were identified in this study that caused performance degradation at high temperatures: (1) morphology transition, (2) change in thickness, (3) burning of CNTs above 500 °C, (4) increment in energy bandgap, (5) fast electron recombination, and (6) poor driving force of injected electrons. This study aims on the influence of thermal treatment on the performance of In_2O_3-SWCNTs-based DSSC. The thermal treatment of the photoanodes was investigated under various annealing temperatures.

Experimental details

Acid treatment of SWCNTs

The single-walled carbon nanotubes (SWCNTs), sulfuric acid (H_2SO_4), and nitric acid (HNO_3) were purchased from Sigma-Aldrich (USA). The SWCNTs were added into the mixture of H_2SO_4/HNO_3 in the ratio of 3:1 and followed by ultrasonication at 30 °C for 1 h. The mixture was then filtered through a membrane filter and washed with ethanol and deionized water to remove the acidity. The cleaned SWCNTs were dried in an oven at 80 °C for 8 h and ground for 30 min to produce homogenous SWCNTs.

Preparation of thin films

The pristine SWCNTs (average diameter of 19 nm), indium chloride ($InCl_3$), and 2-methoxyethanol were purchased from Sigma-Aldrich (USA). Preparation of thin films takes place by sol-gel method through spin-coating technique. A solution of 0.1 M of $InCl_3$ and 2-methoxethanol was prepared by heating it on a hot plate at 60 °C for 24 h. The SWCNTs were added when the aqueous solution turned yellowish gel-like with a continuous stirring for 1 h at 50 °C. The spin-coating process took place by spinning the mixture five times by a spin coater deposited on a clean fluorine-doped tin oxide (FTO)-coated glass substrate. The thin films were then annealed at 400, 450, 500, 550, and 600 °C for 30 min in air to obtain In_2O_3-SWCNTs.

Fabrication of DSSC

The annealed thin films were then immersed with Ruthenium N719 dye (0.5 mM) which acts as a sensitizer in the fabrication of DSSC. The immersion took place for 24 h in a glass petri dish. The immersed substrate thin films were then rinsed with ethanol to remove the excess dye. Simultaneously, a platinum counter electrode was prepared using screen printing technique and annealed at 400 °C for 1 h. The fabrication of DSSC took place by sandwiching the counter electrode and the annealed thin films. Binder clips were used to fix the cell. Electrolyte (Idolyte MPN 100) was injected into the sandwiched cell by forming an active area of 1 cm^2.

Characterization of thin films

Characterization was done onto the photoanodes and DSSC. The photoanodes were characterized by using X-ray diffraction (XRD), filed emission electron microscopy (FESEM), energy dispersive X-ray spectroscopy (EDX), and ultraviolet-visible spectrophotometry (UV-Vis) measurements. The DSSC was characterized by using incident photon-to-current efficiency (IPCE) and electrochemical impedance spectroscopy (EIS) measurements. The morphological properties were analyzed via FESEM (Merlin, Gemini II; 20 V-30 kV) and EDX (ZEISS EVO MA 10 (UK)) measurements. The energy bandgap of the thin films was analyzed by UV-Vis (PERKIN ELMER). Meanwhile, the performance of DSSC was analyzed through IPCE (CEP-2000BX, Bunko-Keiki). The electrochemical properties were obtained from EIS analysis through GAMRY Series G300 Potentiostat-electrochemical impedance.

Experimental results and discussion

X-ray diffraction analysis

Figure 1 shows XRD patterns of In_2O_3 added with 0.3 wt% of SWCNTs at various annealing temperatures of (a) 400 °C, (b) 450 °C, (c) 500 °C, (d) 550 °C, and (e) 600 °C. The diffraction peaks of In_2O_3 were identified at $2\theta = 21.3°$, 30.6°, 33.2°, 35.4°, 37.9°, 41.8°, 45.6°, 48.6°, 51.1°, and 55.9° attributed to *hkl* plane of (211), (222), (321), (400), (411), (332), (431), (521), (440), and (611), respectively. The lattice constant is $a = 10.117$ Å for In_2O_3 crystal with cubic structure (JCPDS number 01-071-2194).

The preferred orientation for In_2O_3 was confirmed at (222) crystal plane. The peak traced at $2\theta = 26.66°$ with (002) plane belongs to carbon from SWCNTs [26]. The peak was not observed at annealing temperatures above 500 °C confirms that burning of SWCNTs occurs at this annealing temperature. Table 1 shows the crystallite size, *D* of the annealed samples. The crystallite size decreased from 400 to 500 °C and increased on the following temperatures. This result indicates that presence of SWCNTs and annealing temperatures influenced the crystallite size of the samples. The increment in crystallite size shows that the enhancement in the crystallinity of the annealed films.

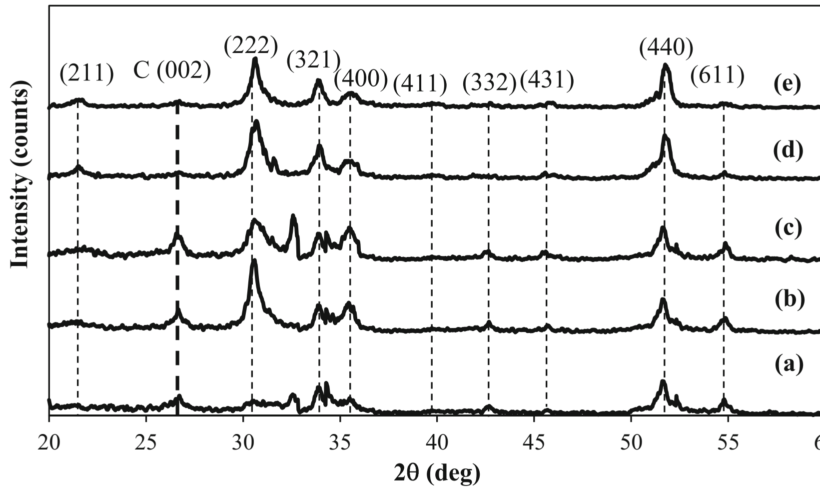

Fig. 1 XRD spectrum of In_2O_3-SWCNTs thin films annealed at (a) 400 °C, (b) 450 °C, (c) 500 °C, (d) 550 °C, and (e) 600 °C

FESEM analysis

Figure 2 shows the FESEM images of In_2O_3-SWCNTs thin films before undergoing annealing treatment. The agglomeration of In_2O_3 and SWCNTs is observed clearly in Fig. 2b. The white patch (circled) in Fig. 2b is the agglomeration of In_2O_3 grains. Besides that, the SWCNTs entangled and covered the In_2O_3.

Figure 3 shows the FESEM images of In_2O_3-SWCNTs thin films annealed at (a) 400 °C, (b) 450 °C, (c) 500 °C, (d) 550 °C, and (e) 600 °C. The annealing treatment shows a good agreement of interaction between In_2O_3 and SWCNTs without agglomeration, where agglomeration may cause DSSC performance deficiency [27]. The annealing process in In_2O_3-SWCNTs changed the size of In_2O_3 grains and shapes of In_2O_3. Lu et al. [27] mentioned that the In_2O_3 grains changes shape from cubic to octahedron as the annealing temperature increases as shown in Fig. 4. Moreover, a previous study acknowledged that annealing treatment promotes morphology transition where shape of particles modifies at higher annealing temperatures [28]. The obtained FESEM result shows that the annealed In_2O_3-SWCNTs thin films morphology transition from spherical to cubic and then to octahedron as the annealing temperature rises from 400 to 600 °C.

The thin film annealed at 400 °C has spherical shaped In_2O_3 grains covered with tiny furs on the surface of the grains. These furs help in greater amount of N719 dye adsorption in order to facilitate photogenerated electrons in DSSC. However, the observed thin film has low porosity where the In_2O_3 grains are compact to each other with less pores. Besides that, the grain sizes are also not uniform with small and large grains of In_2O_3. Morphology transition occurred as the annealing temperature rises to 450 °C with cubic In_2O_3 Fig. 3b. The cubic SWCNTs were surrounded along the cubic grains. The SWCNTs were appeared in a coil like manner forming coiled pores in the thin film. The annealed thin film shows higher porosity and less dense structure.

On the other hand, the SWCNTs in the thin films diminish as the annealing temperature increases from 500 to 600 °C. The residues of SWCNTs that are still connected to the In_2O_3 grains are observed in the thin film annealed at 500 and 550 °C. However, the SWCNTs are not observed in the thin films annealed at 600 °C. This result is due to the burning of SWCNTs at annealing temperature above 500 °C [29].

Besides that, the In_2O_3 grains transformed into octahedron at temperature above 500 °C. The thin film annealed at 500 °C has high porosity with formation of grains in a coil-like structure leaving behind nanometer pores. However, the porosity is lower compared to thin film annealed at 450 °C. A minimum amount of SWCNTs residue is observed in thin film annealed at 550 °C. The burnt SWCNTs left small pores on the surface of In_2O_3 octahedron grains as observed in the magnified image of Fig. 3d. The small tiny pores are the result of SWCNTs penetration into the In_2O_3 grains. The average diameter of these tiny pores is 15 nm which is the average diameter of pristine SWCNTs (19 nm). The annealing process is the reason in the reduction of SWCNTs diameter.

Moreover, the coiled structure observed in the thin films annealed at 450 and 500 °C is not seen in the film annealed at 550 °C. This result proves that addition of SWCNTs is the reason for the formation of coiled structure with nanometer pores. The coiled structure is not observed in the thin film annealed at 600 °C due to the absence of SWCNTs. Furthermore, the thin film annealed at 600 °C shows

Table 1 XRD parameters of annealed In_2O_3-SWCNTs

Annealing temperature (°C)	*hkl*	*2θ* (°)	Crystallite size, *D* (nm)
400	222	30.550	38.20
450	222	30.575	34.36
500	222	30.600	16.38
550	222	30.650	17.64
600	222	30.675	18.22

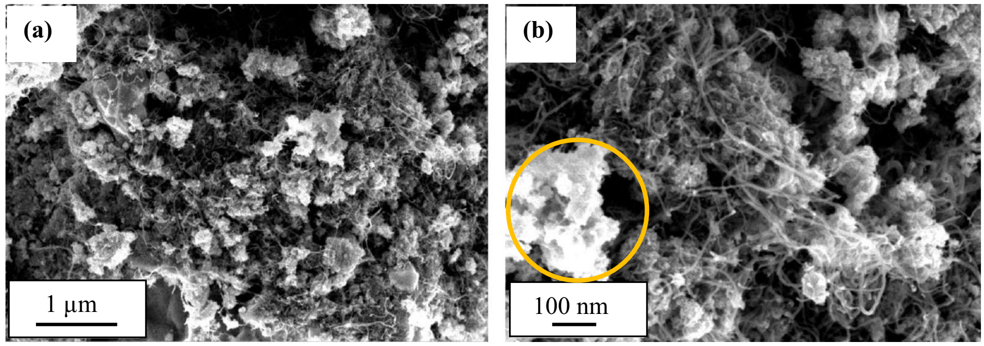

Fig. 2 FESEM images of In_2O_3-SWCNTs before annealing in scale of **a** micron and **b** nano

octahedron In_2O_3 denser grains with low porosity. However, the tiny pores on the surface of In_2O_3 octahedron grains were not observed in the film annealed at 600 °C. The In_2O_3 octahedron grains have smooth surface morphology. This is due to the role of annealing treatment where annealing process can enhance the morphology of thin films [30]. The FESEM images show that the porosity reduces above annealing temperature of 500 °C due to the decreasing formation of coil-like structure in the thin films.

The average size of In_2O_3 particles influenced by annealing temperature is tabulated in Table 2. Although annealing treatment caused the average size of particles to reduce, the thin film annealed at 450 °C has smaller size of particles than that of 500 °C. This is due to the cubic structure (450 °C) with

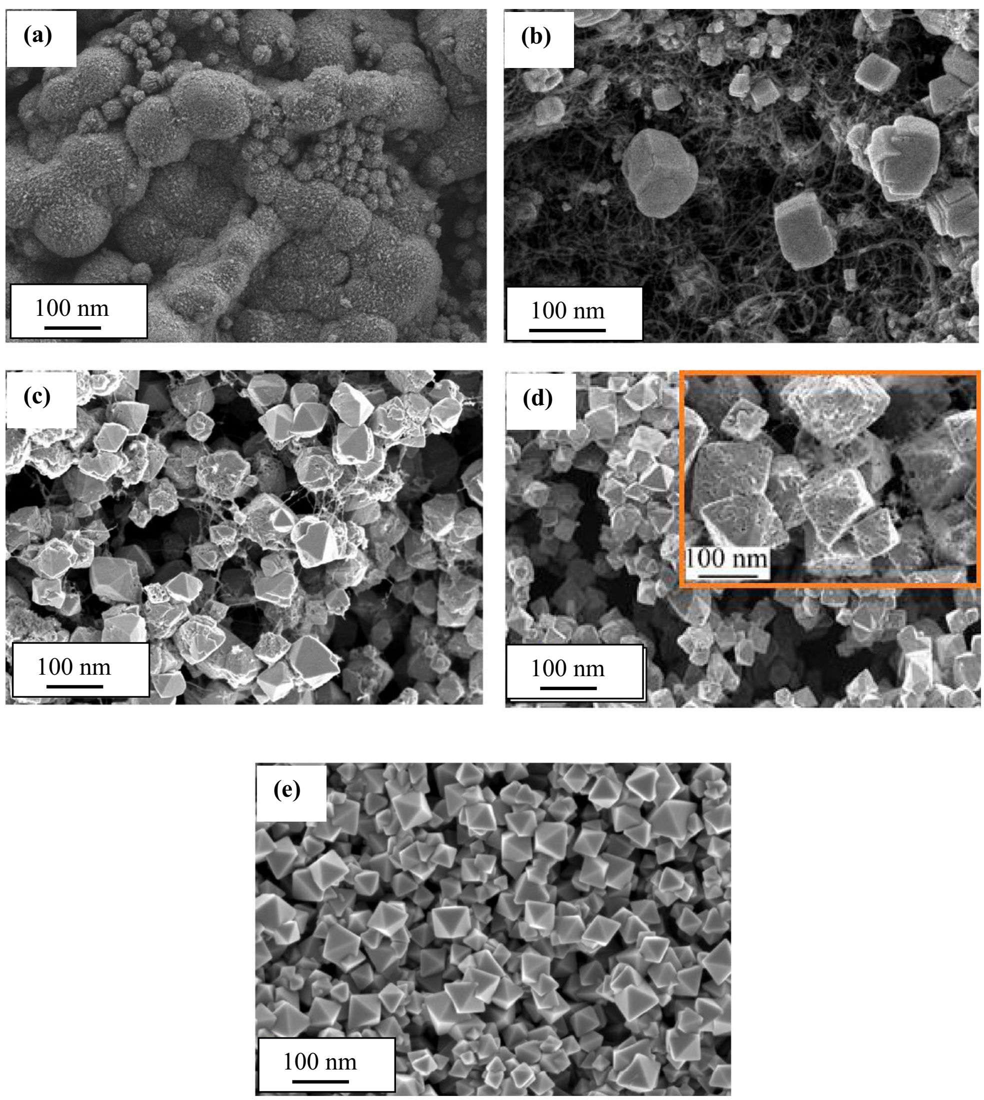

Fig. 3 FESEM images of In_2O_3-SWCNTs thin films annealed at **a** 400 °C, **b** 450 °C, **c** 500 °C, **d** 550 °C, and **e** 600 °C

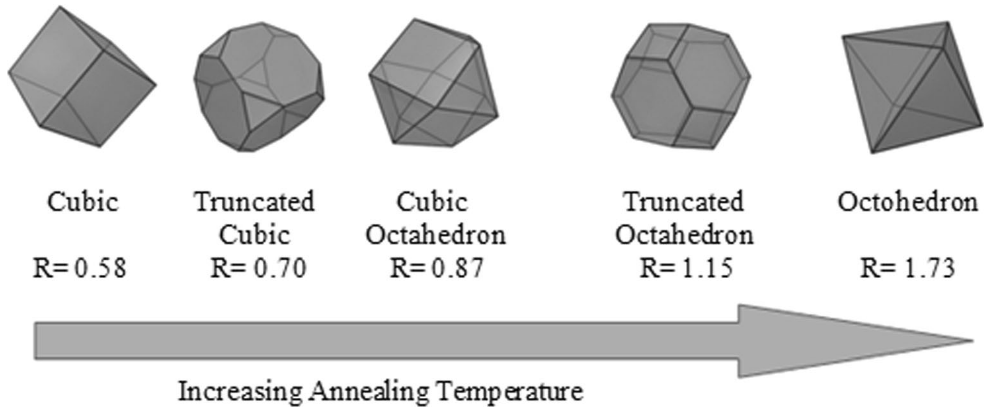

Fig. 4 Phase transformation of In_2O_3 as the annealing temperature increases

smaller radius than the octahedron structure (500 °C) with R = 0.58 and R = 1.73, respectively [27]. The size of octahedron particles decreased from 500 to 600 °C because of increment in annealing temperature. Moreover, previous literature reported that annealing temperature is the key factor that influenced the size of particles to decrease [31]. Furthermore, the small particle size provides large surface area for efficient dye adsorption.

Figure 5 demonstrates the thickness of In_2O_3-SWCNTs thin films. The average thickness of the thin films is listed in Table 2. The average thickness of In_2O_3-SWCNTs thin films annealed at 400, 450, 500, 550, and 600 °C are 1.9, 1.8, 1.5, 0.9, and 0.4 μm, respectively. The thickness of the thin films decreased as the annealing temperature increases. This phenomenon occurred due to the compact nature of the thin films as the temperature rises as seen in Fig. 3. A suitable thickness is important to adsorb light by the N719 dye molecules [32]. Thin film that is too thick or incredibly thin may increase the rate of electron recombination and decrease the efficiency of DSSC [33].

EDX analysis

Figure 6 shows the EDX analysis of In_2O_3-SWCNTs thin films. The weight percentage and atomic percentage of the elements are listed in Table 3. The EDX spectrum reveals that the annealed thin films have element composition of indium (In), oxygen (O), and carbon (C) without other impurities in the thin film. The result shows that the atomic percentage increases as the annealing temperature rises. Meanwhile, the atomic percentage of indium increases as the annealing temperature increases indicating that the surface area of In_2O_3 increases with rising temperature [34]. On the other hand, the atomic percentage of carbon decreases as the annealing temperature increases. A very low amount of atomic percentage of carbon (6.01%) is observed at thin film annealed at 500 °C and the presence of carbon element is not seen in the thin films annealed at 550 and 600 °C. This result proves that SWCNTs tend to burn at temperature above 500 °C as observed in the FESEM images (Fig. 3).

UV-Vis analysis

Figure 7 shows graph of $(\alpha hv)^2$ function of photon energy, hv to obtain the energy bandgap (E_g) for the annealed thin films. The E_g can be measured using the following equation [35, 36]:

$$(\alpha hv)^2 = A^2\left(hv - E_g\right) \tag{1}$$

where α an A are the optical absorption coefficients and constant value, respectively.

The energy bandgap values are listed in Table 2. The decrement of bandgap from 400 to 500 °C is due to the bonding formation of In-O-C due to the change in covalent bonding caused by the addition of acid in SWCNTs that leads to interference in the aromatic system, which in turn changes the energy level of CNTs [37, 38]. However, the energy bandgap increased for thin films annealed above 500 °C where the CNTs tend to burn at this temperature. The result reveals that

Table 2 Average size of particles, thickness, energy bandgap, IPCE, and charge collection efficiency (η_{coll}) for annealed In_2O_3-SWCNTs thin films

Annealing temperature (°C)	Average size of particles (nm)	Thickness (μm)	Energy bandgap (eV)	IPCE (%)	η_{coll} (%)
400	136	1.9	3.25	23	90.79
450	73	1.8	3.00	29	99.96
500	87	1.5	2.62	27	96.96
550	74	0.9	2.93	22	(Undesired case)
600	65	0.4	3.37	21	(Undesired case)

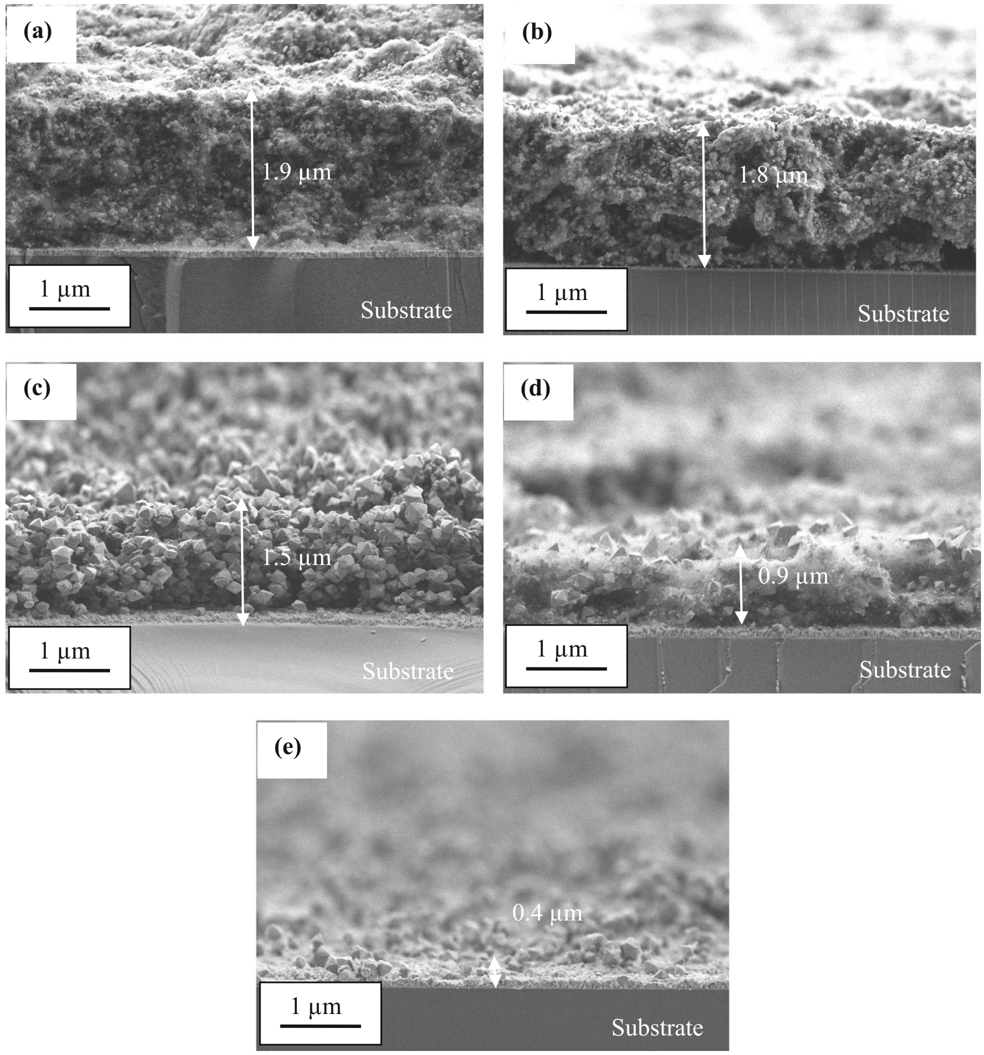

Fig. 5 FESEM images with thickness of In_2O_3-SWCNTs thin films annealed at **a** 400 °C, **b** 450 °C, **c** 500 °C, **d** 550 °C, and **e** 600 °C

the presence of acid-treated SWCNTs was able to decrease the energy bandgap of the photoanodes.

Furthermore, low value of E_g causes high probability of the injected electron in the conduction band (CB) of metal oxide semiconductor to be excited into the valence band. However, a very small E_g value obtained by thin film annealed at 500 °C may interrupt the excitation process of injected electron as it acts as conductor material and not semiconductor material. Hence, the thin films annealed at 450 °C achieved the optimum energy bandgap of 3.00 eV.

IPCE performance

Figure 8 shows the IPCE curve for In_2O_3-SWCNTs-based DSSC. IPCE analysis determines the performance of DSSC. Table 2 tabulates the percentage value of IPCE for In_2O_3-SWCNTs-based DSSC. The morphology-dependent IPCE performance is shown clearly in Fig. 9. IPCE curve explains the ratio of electrons obtained towards the total number of photon received by DSSC at a certain wavelength. Baxter et al. stated that photon conversion by dye molecules occurs at wavelength range of 450–570 nm [39]. The result obtained also shows high peaks ranging from 450 to 570 nm which is inclined with the previous literature in [39]. Besides that, the optimum quantum efficiency of N719 sensitized cells is maximized at 525 nm, which attributes to the N719 adsorption peak.

The IPCE performance is influenced by three main parameters: (1) light harvesting efficiency (LHE), electron injection efficiency (η_{inj}), and the collection efficiency (η_{coll}). The IPCE performance can be measured by the following equation [39].

$$\mathrm{IPCE} = \mathrm{LHE} \times \eta_{inj} \times \eta_{coll} \quad (2)$$

where the LHE is directly connected to the degree of dye loading, η_{inj} is the efficiency of the injected electron from the excited dye to the conduction band of In_2O_3-SWCNTs and η_{coll} is the efficiency of the injected electron at the back contact.

Since the *LHE* values are dependent on the degree of dye loading, the measured results show that the number of

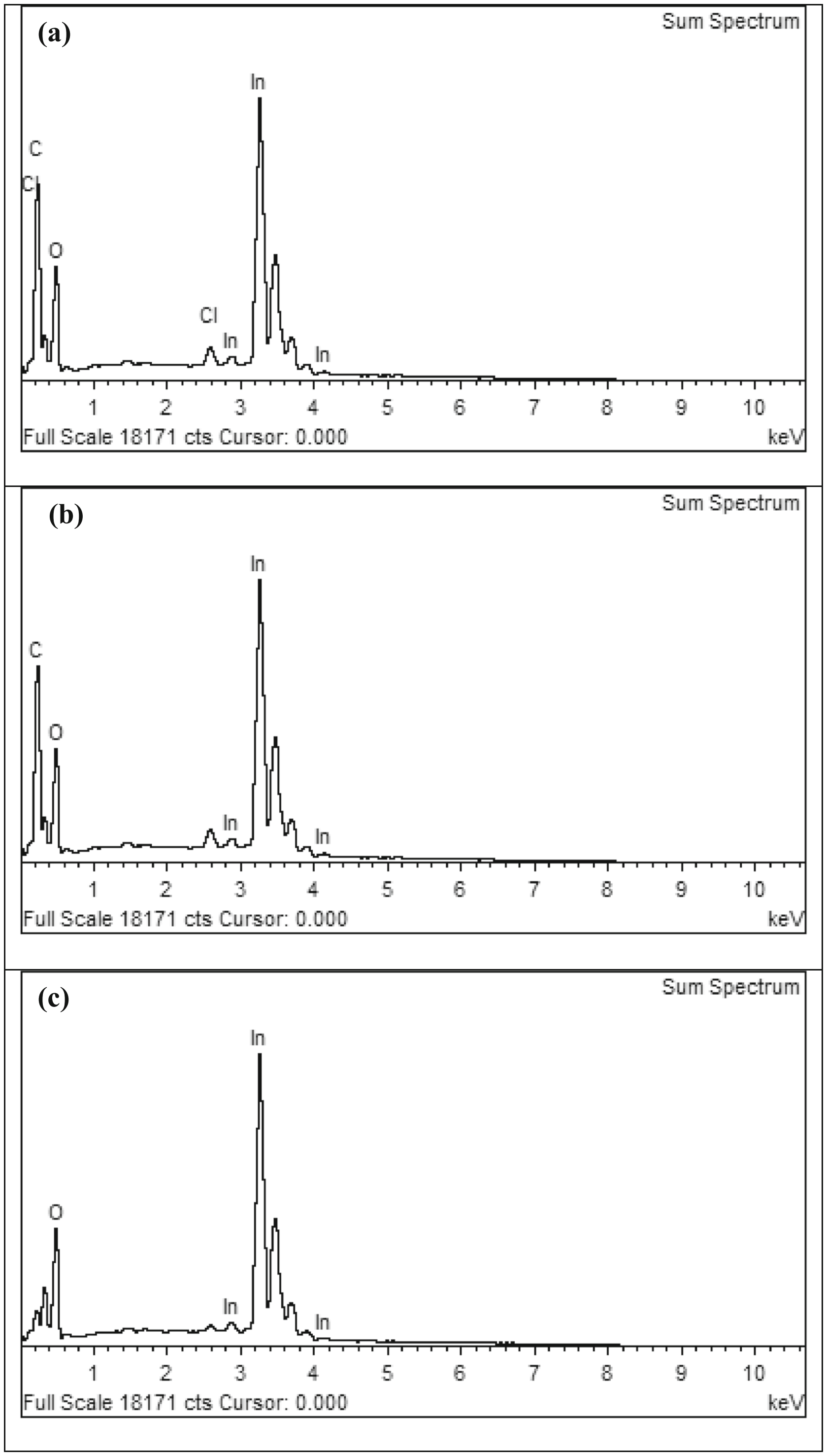

Fig. 6 EDX images of In_2O_3-SWCNTs thin films annealed at **a** 400 °C, **b** 450 °C, **c** 500 °C, **d** 550 °C, and **e** 600 °C

molecules adsorbed on thin films annealed at 400, 450, 500, 550, and 600 °C are 1.08×10^{-7}, 1.15×10^{-7}, 1.10×10^{-7}, 1.11×10^{-7}, and 1.18×10^{-7} mol cm^{-2}, respectively. The dye adsorption result denotes accordingly to the average particle size and thickness of annealed In_2O_3-SWCNTs (Tables 1 and 2). The thin film consisting smaller particles with larger surface area have greater amount of dye adsorption, where the thin film annealed at 600 °C with smallest average particle size of 65 nm has the greatest amount dye adsorption of 1.18×10^{-7} mol cm^{-2}. However, the increment in dye adsorption does not correspond with the values of IPCE as in Table 2. The thin film annealed at 600 °C with greatest amount dye adsorption has

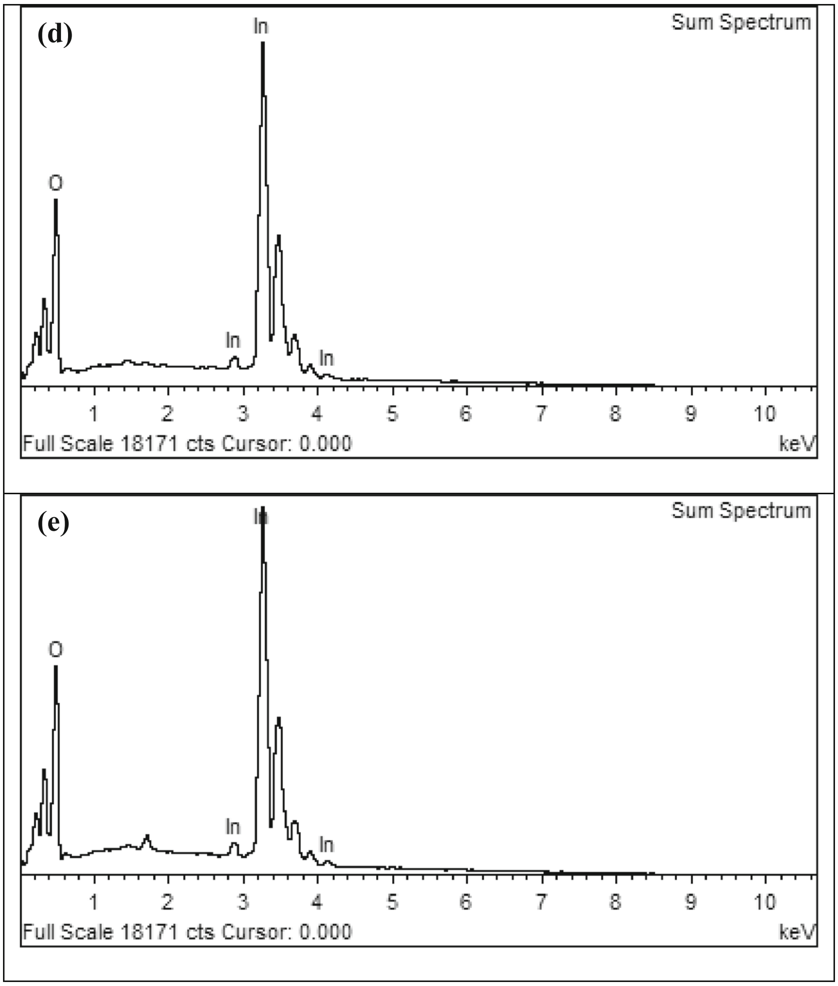

Fig. 6 (continued)

the lowest IPCE value of 21%. Thus, the result indicates that LHE is not the main factor influencing the performance of DSSC. Other factors such as η_{inj} and η_{coll} are the primary factors that affect the IPCE performance of DSSC.

The η_{inj} depends on the driving force of the injected electron. In order to have an efficient η_{inj}, the energy variation between the lowest energy unoccupied molecular orbital (LUMO) of N719 and the conduction band edge (E_{CB}) of the semiconductor must be high. According to the UV-Vis analysis, the E_{CB} of the In_2O_3-SWCNTs thin films can be approximately obtained from the energy bandgap of the In_2O_3-SWCNTs. As observed from UV-Vis analysis (Fig. 7), the addition of SWCNTs in In_2O_3 matrix modified the energy level of the photoanodes. The decrement in bandgap is due to the change in E_{CB} of the photoanodes. According to Hara et al., the E_{CB} of In_2O_3 is 0.5 eV vs. NHE [40]. The addition of SWCNTs in In_2O_3 matrix caused decrement in the energy bandgap of the photoanodes as observed in Fig. 7. This event causes the flat band potential (E_{FB}) to shift downwards towards the positive potential. The positive shift of E_{FB}

Table 3 Weight and atomic percentage of In_2O_3-SWCNTs thin films

Annealing temperature (°C)	Weight percentage (%)			Atomic percentage (%)		
	In	O	C	In	O	C
400	57.01	11.29	31.70	12.92	18.37	68.70
450	75.09	16.05	8.86	27.30	41.89	30.81
500	80.25	18.33	1.42	35.61	58.38	6.01
550	91.16	8.84	–	58.97	41.03	–
600	80.63	19.37	–	36.71	63.29	–

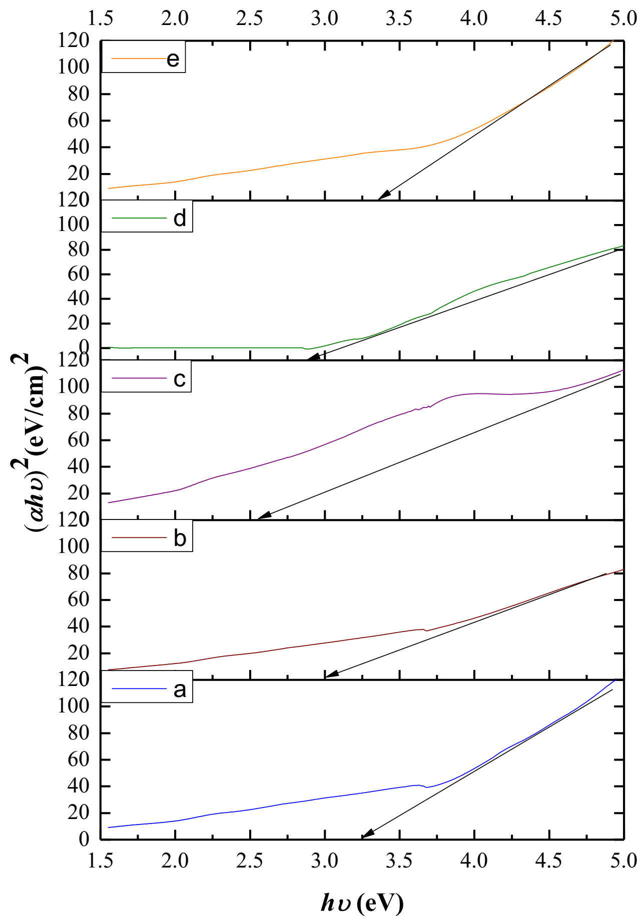

Fig. 7 Graph of $(\alpha h\nu)^2$ vs. $h\nu$ of In_2O_3-SWCNTs thin films annealed at (a) 400 °C, (b) 450 °C, (c) 500 °C, (d) 550 °C, and (e) 600 °C

increases the energy gap between the LUMO of N719 and the CB of In_2O_3-SWCNTs. Therefore, smaller energy bandgap of photoanodes favor the injected electrons with higher driving force to the CB of the photoanode, which in turn increases the electron injection efficiency from the LUMO of dye to the In_2O_3-SWCNTs CB. The η_{coll} is associated with the ratio of charge transport and charge recombination that can be determined from the EIS parameters.

The result shows the IPCE curve increased from 400 to 450 °C and decreased as the annealing temperature rises. The photoanode annealed at 450 °C exhibits the highest photon conversion efficiency of 29%. This result is supported by the formation of cubic In_2O_3 structure, where Gan et al. mentioned that cubic In_2O_3 may increase the electrical conductivity and allows an efficient path for electron mobility [28]. In addition to that, In_2O_3-SWCNTS (450 °C) achieved greater value of IPCE than the surfactant modified In_2O_3 with 28% demonstrated in [41]. Besides that, the photoanode achieved the optimum thickness of 1.8 μm by reducing the electron recombination that occurs in the DSSC. The formation of coiled pores due to addition of SWCNTs increases the porosity of the photoanode allowing more photon to adsorb by the N719 dye molecules. In addition to that, the SWCNTs are capable of absorbing visible light [28]. Therefore, the contribution of SWCNTs to light conversion cannot be ignored. Thus, the percentage of IPCE increased for the photoanode annealed at 450 °C.

Furthermore, the photoanode annealed at 400 °C exhibits 23% of IPCE. Although the growth of furs on the surface of spherical In_2O_3 grains may assist in efficient dye adsorption, the performance of DSSC is still low. This is due to the low porosity in the photoanode with compact grains and less pores as seen in the FESEM image (Fig. 3a). The IPCE result denotes that the spherical In_2O_3 grains with tiny furs adsorb large amount of dye molecules but failed to capture the photon energy for conversion due to low porosity of the photoanode.

Even though the photoanode annealed at 500 °C possesses high porosity with formation of grains in a coil-like structure leaving nanometer pores, the performance of DSSC was still lower than that of 450 °C. This photoanode achieved the second highest value of IPCE after the photoanode annealed at

Fig. 8 IPCE curve of In_2O_3-SWCNTs-based DSSC for photoanode annealed at (a) 400 °C, (b) 450 °C, (c) 500 °C, (d) 550 °C, and (e) 600 °C

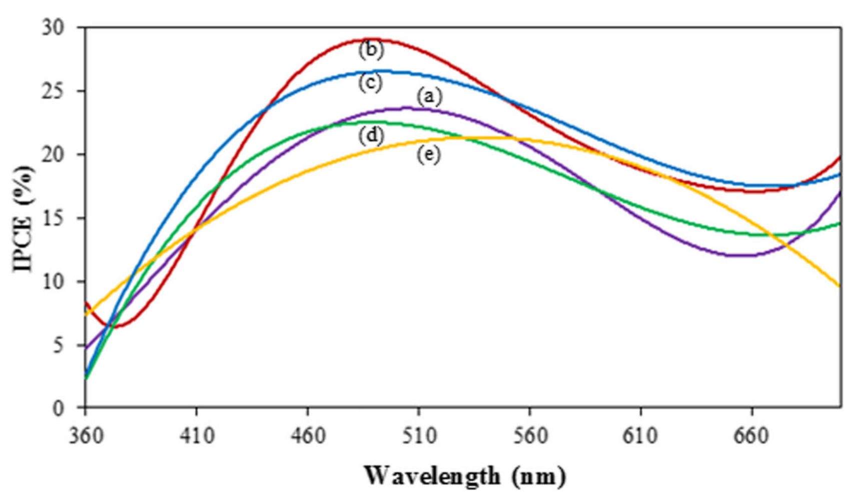

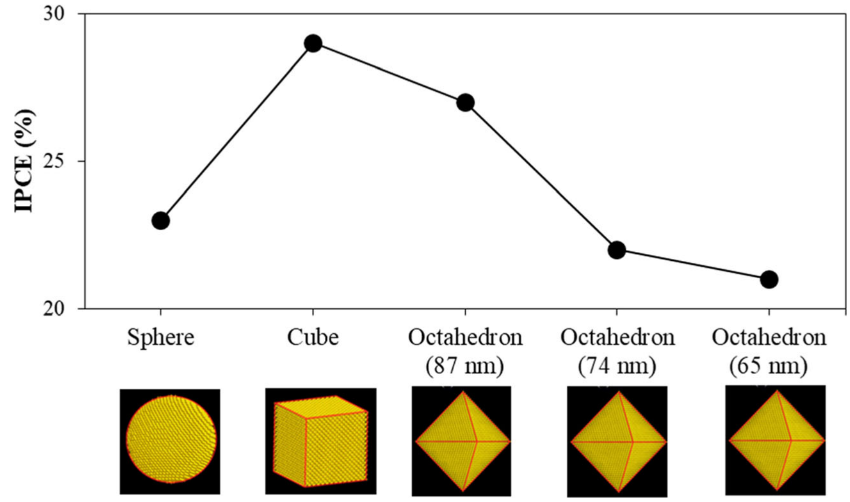

Fig. 9 IPCE Performance of In_2O_3-SWCNTs-based DSSC depending on morphology

450 °C. This is due to the burning of SWCNTs above 500 °C observed in the FESEM and EDX images. This result indicates that the presence of SWCNTs influences more on the performance of DSSC than the porosity. The residues of SWCNTs connected to the In_2O_3 grains may interrupt the electron transport path in DSSC causing high rate of electron recombination. Owing to that, the IPCE value may decrease at annealing temperature of 500 °C.

Meanwhile, the photoanode annealed at 550 °C exhibits low value of IPCE due to the minimum amount of SWCNTs in the photoanode. The tiny pores left as former marks of SWCNTs penetration on surface of In_2O_3 grains provides small amount of porosity to the photoanode. However, the SWCNTs play a major role than the porosity in DSSC. Hence, the low porosity, absence of SWCNTs, and deformation of coil-like structure caused the photoanode annealed at 550 °C display a low performance.

Moreover, the photoanode annealed at 600 °C has the lowest IPCE. Even though the octahedron grains were formed smoothly without tiny pores as a result of former marks of SWCNTs penetration and large surface area due to formation of small particles and has the greatest amount dye adsorption (1.18×10^{-7} mol cm^{-2}), yet the DSSC performance was low. This is due to the absence of SWCNTs with the lowest porosity causing less photon conversion that may inhibit and decrease the performance of DSSC.

Photovoltaic performance

Figure 10 shows the *J*–*V* curve of In_2O_3-SWCNTs DSSC annealed at various annealing temperatures. Table 4 shows the photovoltaic performance of annealed In_2O_3-SWCNTs DSSCs. The photocurrent density (J_{sc}) is the maximum current density value achieved when the cell is short circuited. The open circuit voltage (V_{oc}) is given by the potential difference in the electrolyte. The fill factor (*FF*) is defined as the ratio between the maximum cell output power and the product of V_{oc}

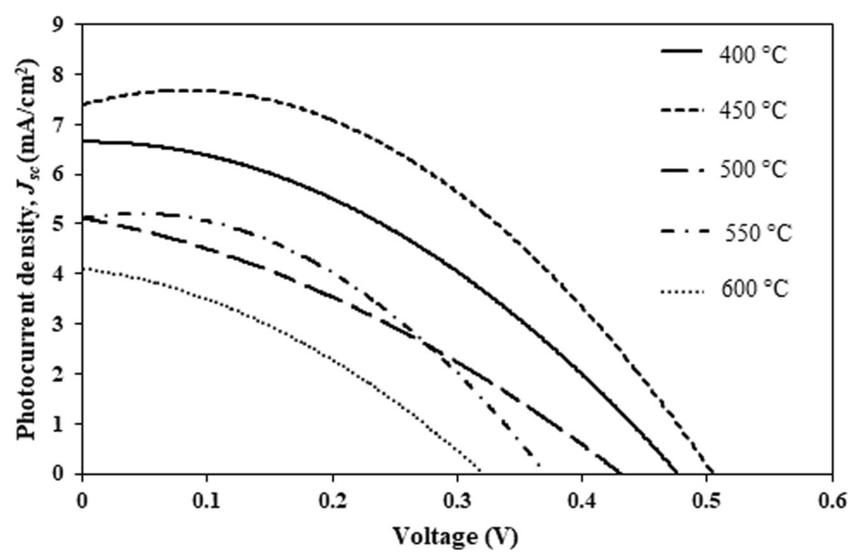

Fig. 10 *J*–*V* curves of In_2O_3-SWCNTs-based DSSC after annealed at 400, 450, 500, 550, and 600 °C

Table 4 Photovoltaic performances of In_2O_3-SWCNTs-based DSSC

Annealing temperature (°C)	J_{sc} (mA/cm^2)	V_{oc} (V)	*FF*	η (%)
400	6.78	0.48	0.31	1.00
450	7.52	0.51	0.36	1.41
500	5.12	0.43	0.32	0.71
550	4.22	0.37	0.35	0.56
600	4.10	0.32	0.29	0.38

with J_{sc}. The energy conversion efficiency of the solar cell was calculated by [4]:

$$\eta = \frac{V_{oc} J_{sc} FF}{P_{in}} \tag{3}$$

where P_{in} is the optical power of 100 mW/cm^2 under AM 1.5.

J_{sc} significantly increased from 400 to 450 °C and decreased on the following annealing temperatures as seen in Table 4. Due to the increase of J_{sc}, the power conversion efficiency (PCE) also increases from 1.00 to 1.41% for the respective photoanodes. We also observed that In_2O_3-SWCNTs-450 °C has the highest *FF* among the photoanodes. Mahalingam et al. mentioned that *FF* is mainly affected by internal resistance at interface of FTO/photoanode, platinum/electrolyte, and FTO [8]. High *FF* in In_2O_3-SWCNTs-450 °C is due to the decrease in series resistance (R_s) which is described in detail in EIS analysis. The high electron recombination rate may cause the low *FF* and affects the PCE in In_2O_3-SWCNTs-600 °C. Moreover, the In_2O_3 thin films without the addition of SWCNTs demonstrated in our previous work showed lower PCE of 0.21% [9]. The increment in PCE after addition of SWCNTs indicates performance enhancement after addition of SWCNTs in In_2O_3.

Electron transport analysis

The EIS analyzes the effect of interface modification on the electron mobility and recombination kinetics of the DSSC. Figure 11 shows the EIS spectra of the annealed photoanodes with fitted curves. The EIS spectra were fitted based on a transmission line circuit as seen in Fig. 12. The model represents the actual structure of DSSC system including resistances and capacitances. The resistances consist of sheet resistance (R_s), substrate resistance (R_{FTO}), transport resistance (R_t), charge transfer resistance (R_{ct}), counter electrode resistance (R_{pt}), and Warburg impedance (Z_D). Meanwhile, the capacitances consist of substrate capacitance (C_{FTO}), chemical capacitance (C_{μ}), and Helmholtz capacitance (C_{pt}).

R_t reflects to the diffusion in the photoanode/electrolyte interface. R_{ct} corresponds to the recombination at the photoanode/dye/electrolyte interface. The EIS data obtained from the fitted curves determines the electron lifetime (τ_{eff}), effective rate constant (k_{eff}), effective electron diffusion coefficient (D_{eff}), and effective electron diffusion length (L_n) and can be calculated from the following equations [42, 43].

$$\tau_{eff} = \frac{1}{2\pi f_{max}} \tag{3}$$

$$k_{eff} = \frac{1}{\tau_{eff}} \tag{4}$$

$$D_{eff} = \frac{R_{ct} L^2}{R_t \tau_{eff}} \tag{5}$$

$$L_n = D_{eff} \tau_{eff} \tag{6}$$

where f_{max} is the maximum frequency of the fitted curve of EIS spectrum and L is the length of the photoanode measured through FESEM (Fig. 5). The electron transport parameters obtained from the fitted EIS spectra are listed in Table 5.

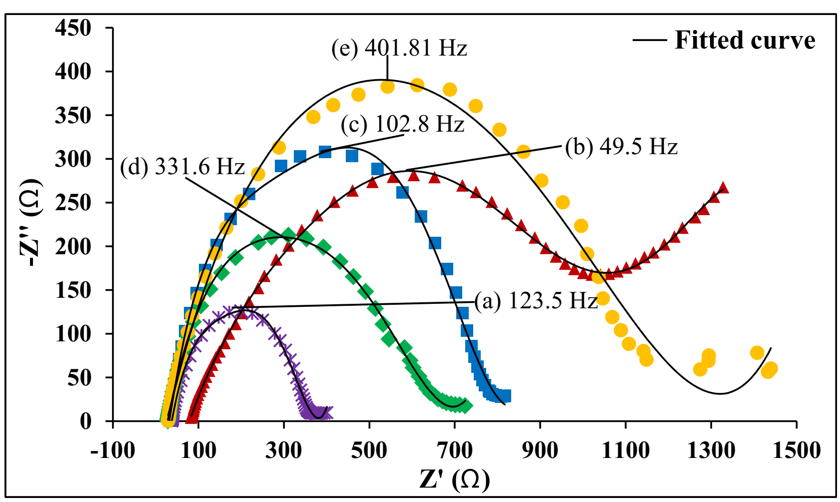

Fig. 11 EIS spectra of In_2O_3-SWCNTs-based DSSC with fitted curves annealed at (a) 400 °C, (b) 450 °C, (c) 500 °C, (d) 550 °C, and (e) 600 °C

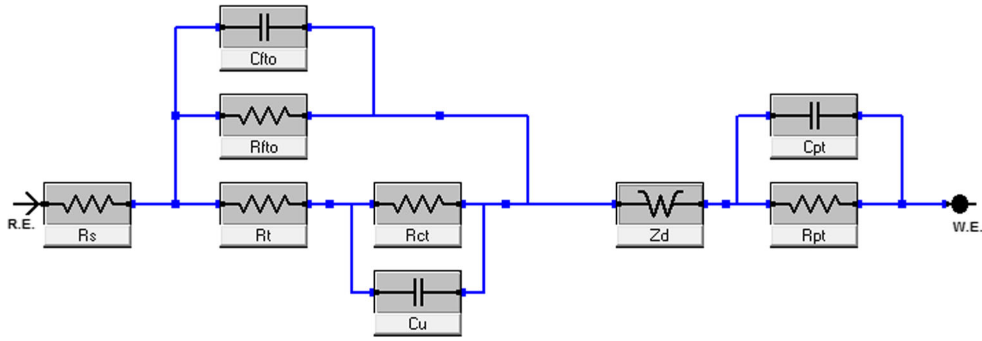

Fig. 12 Transmission line model for EIS data fitting

The R_s values reflect the ohmic resistance of the counter electrode [44]. The photoanode annealed at 450 °C with cubic structure has the smallest R_s value of 31.7 Ω, indicating that it has higher electrical conductivity than the other photoanodes. The R_s values are increased as the annealing temperature increased above 500 °C may be due to the bandgap enlargement as seen in the UV-Vis analysis denoting that the electrical conductivity decreased [45]. In addition, Hara et al. mentioned that low R_s will cause higher driving force for electron injection and increases the η_{inj} [46].

Furthermore, for a desired case of DSSC, the photoanode should have longer electron diffusion length than the photoanode thickness ($L_n >> L$) and larger recombination charge transfer resistance than the transport resistance ($R_{ct} >> R_t$). However, the photoanodes annealed at 550 and 600 °C shows an undesired case where the transport resistance is greater than the recombination charge transfer resistance ($R_{ct} << R_t$). This phenomenon is called as Gerischer impedance that causes the injected electrons to be diffused earlier before reaching the FTO glass substrate by the tri-iodite reaction [47]. Thus, weaker diffusion impact than recombination impact accelerates the IPCE performance of In_2O_3-SWCNT-based DSSC.

Moreover, larger R_{ct} indicates that slow recombination effect takes place inside the DSSC. Meanwhile, lower R_t causes smaller electron-hole recombination effect. The k_{eff} implies the rate of electron recombination in DSSC. The thin film annealed at 450 °C (cubic structure) exhibits the lowest electron recombination rate of 311.06 s^{-1} with the greatest R_{ct} (524.74 Ω) and the lowest R_t (0.22 Ω). As mentioned above, η_{coll} is associated with the ratio of charge transport and charge recombination. High charge collection efficiency is obtained when electrons are injected with large driving force to the CB of the photoanode with high electron injection efficiency from the LUMO of dye to the In_2O_3-SWCNTs CB as seen in Scheme 1. The charge collection efficiency can be calculated by the following equation [42].

$$\eta_{coll} = \left(1 - \frac{R_t}{R_{ct}}\right) \times 100 \quad (7)$$

Table 2 shows the charge collection efficiency of the photoanodes. The values of η_{coll} corresponds accordingly to the values of IPCE in the order of 450 °C > 500 °C > 400 °C > 550 °C > 600 °C. The result reveals that large η_{inj} leads to greater η_{coll}. The result also indicates that the performance of DSSC does not solely depends on the light harvesting efficiency (LHE) but on other factors as well such as electron recombination rate, electron lifetime, diffusion effect, and driving force of injected electron. The photoanode annealed at 550 and 600 °C showed undesired cases for DSSC as the transport resistance is higher than the recombination resistance (R_{ct}). Thus, the electron resists to transport smoothly as it is more prone to recombine at the back contact due to the low resistance of R_{ct}.

Besides that, the presence of SWCNTs in the photoanode also strongly influences the recombination kinetics in the DSSC mechanism. The photoanodes annealed above 500 °C showed greater electron recombination rate where the k_{eff} decreased from 400 to 450 °C and increased from 500 to 600 °C due to the burning of SWCNTs above 500 °C as observed in the FESEM images (Fig. 3). Although the maximum amount of dye adsorbed is by the photoanode annealed at 600 °C, it showed the smallest R_{ct} with the highest electron recombination rate of 2524.97 s^{-1}. This result reveals that even though

Table 5 Electron transport properties of the fitted EIS data

Temperature (°C)	L (μm)	f_{max} (Hz)	R_s (Ω)	R_{ct} (Ω)	R_t (Ω)	τ_{eff} (ms)	k_{eff} (s^{-1})	D_{eff} (cm^2 s^{-1})	L_n (μm)
400	1.9	123.5	86.51	367.11	33.80	1.29	776.07	0.00012	3.95
450	1.8	49.5	31.70	524.74	0.22	3.21	311.06	0.0189	78.14
500	1.5	102.8	71.55	401.35	12.21	1.55	645.99	0.00069	10.32
550	0.9	331.6	66.98	63.68	228.52	0.48	2083.77	0.00015	2.76
600	0.4	401.81	87.44	42. 97	123.77	0.40	2524.97	0.00003	1.12

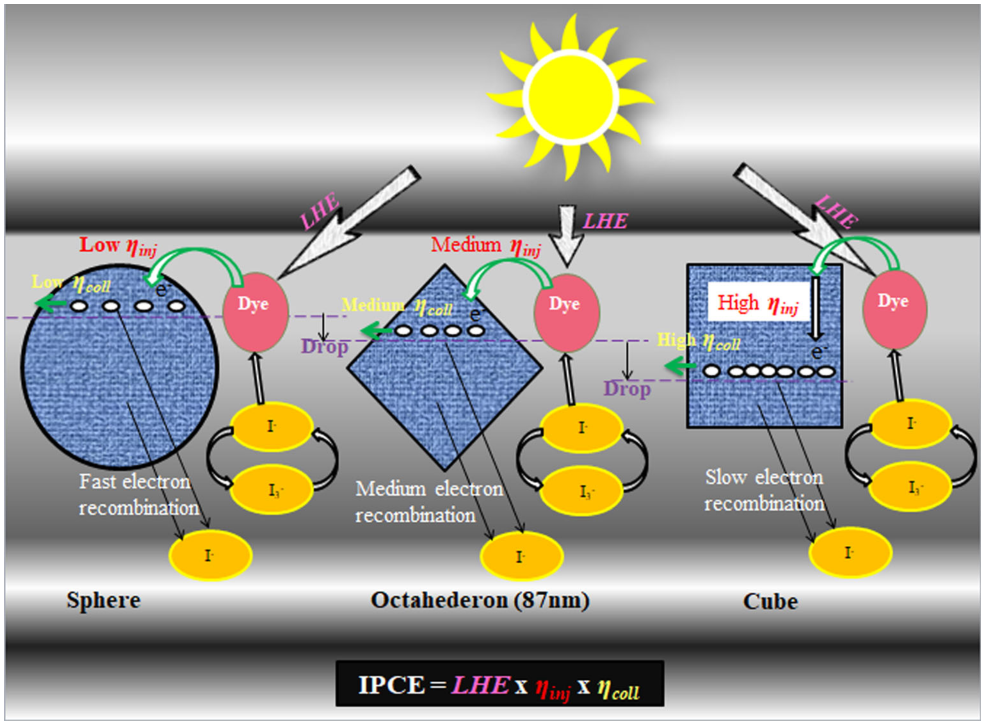

Scheme 1 Morphology-dependent electron recombination rate

the octahedron structure (600 °C) was able to adsorb more dye molecules, the poor electron injection efficiency increased the electron recombination rate and decreased the charge collection efficiency. On that account, the IPCE value of the In_2O_3-SWCNTs (600 °C)-based DSSC decreases to 21% (Table 5).

Moreover, the cubic structure-based photoanode (450 °C) increased electron lifetime (3.21 ms) and effective diffusion coefficient (0.0189 $cm^2\ s^{-1}$) in the cell, and thus improves the IPCE performance of the DSSC. In addition, the D_{eff} increased from 400 to 450 °C and decreased on the following annealing temperatures where the SWCNTs tend to burn. The result signifies that the presence of one-dimensional tube of SWCNTs promotes injected electrons to diffuse smoothly towards the electrode. Hence, large D_{eff} enables to slow down the recombination rate and increases the charge collection efficiency of the DSSC. Therefore, the cubic structure-based photoanode (450 °C) exhibited better electron transport with larger driving force on injected electron (η_{inj}) that decreased the electron recombination rate and electron lifetime and subsequently increased the charge collection efficiency (η_{coll}). Consequently, the IPCE performance of DSSC was enhanced.

Conclusion

In conclusion, the morphological properties of In_2O_3-SWCNTs for DSSC application were successfully studied. The performance of In_2O_3-SWCNTs-based DSSC strongly depends on the annealing temperature. The FESEM result reveals the morphology transition of In_2O_3 grains from spherical to cubic and then to octahedron as the annealing temperature increases. The addition of SWCNTs forms a coil-like structure with nanometer pores in the thin films. This coil-like structure with pores increases the porosity in the thin film. The photoanode annealed at 450 °C exhibited the highest IPCE of 29% owing to its high porosity with greater amount of pores, large surface area with small particle size, and optimum thickness. Although the photoanode annealed at 500 and 550 °C has high porosity, the diminishing SWCNTS due to burning interrupted the electron transport and caused high electron recombination rate in the DSSC. The photoanode annealed at 600 °C showed the lowest performance of 21% of IPCE denoting to the absence of SWCNTs and compact grains with low porosity. However, the IPCE value does not solely depend on the dye adsorption of photoanodes but the η_{inj} and η_{coll}. Smaller energy bandgap of photoanodes favors the injected electrons with higher driving force to the conduction band (CB) of the photoanode, which in turn increases the η_{inj} from the LUMO of dye to the In_2O_3-SWCNTs CB. Besides that, the absence of SWCNTs above 500 °C caused the energy bandgap to increase and leads to lower driving force of injected electrons. Therefore, the cubic structure-based photoanode (450 °C) exhibited better electron transport with larger driving force on injected electron (greater η_{inj}) that decreased the electron recombination rate and increased electron lifetime and subsequently obtained larger η_{coll}. Hence, the IPCE performance of DSSC was enhanced.

References

1. O'Regan B, Grätzel M (1991) A low-cost, high-efficiency solar cell based on dye-sensitized colloidal TiO_2 films. Nature 353:737–740
2. Mahalingam S, Abdullah H, Ashaari I, Shaari S, Muchtar A (2016) Optical, morphology and electrical properties of In_2O_3 incorporating acid-treated single-walled carbon nanotubes based DSSC. J Phys D Appl Phys 49:075601
3. Mahalingam S, Abdullah H, Razali MZ, Yarmo MA, Shaari S, Omar A (2016) Structural, morphological, photovoltaic and electron transport properties of ZnO based DSSC with different concentrations of MWCNTs. Mater Sci Forum 846
4. Abdullah H, Atiqah NA, Omar A, Asshaari I, Mahalingam S, Razali Z, Shaari S, Mandeep JS, Misran H (2015) Structural, morphological, electrical and electron transport studies in ZnO–rGO (wt%= 0.01, 0.05 and 0.1) based dye-sensitized solar cell. J Mater Sci-Mater Electron 26:2263–2270
5. Mahalingam S, Abdullah H, Omar A, Nawi NAM, Shaari S, Muchtar A, Asshari I (2016) Effect of morphology on SnO_2/MWCNT-based DSSC performance with various annealing temperatures. Adv Mater Res 1107:649
6. Abdullah H, Yunos NH, Mahalingam S, Ahmad M, Yuliarto B (2017) Photovoltaic and EIS performance of SnO_2/SWCNTS based–sensitized solar cell. Procedia Engineer 170:1–7
7. Mahalingam S, Abdullah H, Shaari S, Muchtar A (2016) Morphological and electron mobility studies in nanograss In_2O_3 DSSC incorporating multi-walled carbon nanotubes. Ionics 22:1985–1997
8. Mahalingam S, Abdullah H, Manap A (2018) Role of acid-treated CNTs in chemical and electrochemical impedance study of dye-sensitised solar cell. Electrochim Acta 264:275–283
9. Mahalingam S, Abdullah H, Shaari S, Muchtar A, Asshari I (2015) Structural, morphological, and electron transport studies of annealing dependent In_2O_3 dye-sensitized solar cell. Sci World J 2015
10. Liu T, Yu K, Gao L, Chen H, Wang N, Hao L, Li T, He H, Guo Z (2017) A graphene quantum dot decorated $SrRuO_3$ mesoporous film as an efficient counter electrode for high-performance dye-sensitized solar cells. J Mater Chem A 5(34):17848–17855
11. Mori S, Asano A (2010) Light intensity independent electron transport and slow charge recombination in dye-sensitized In_2O_3 solar cells: in contrast to the case of TiO_2. J Phys Chem C 114:13113–13117
12. Mahalingam S, Abdullah H (2016) Electron transport study of indium oxide as photoanode in DSSCs: a review. Renew Sust Energ Rev 63:245–255
13. Hou Q, Ren J, Chen H, Yang P, Shao Q, Zhao M, Zhao X, He H, Wang N, Luo Q, Guo Z (2018) Synergistic hematite-fullerene electron-extracting layers for improved efficiency and stability in perovskite solar cells. Chem Electro Chem 5:72–731
14. Luo Q, Ma H, Hou Q, Li Y, Ren J, Dai X, Yao Z, Zhou Y, Xiang L, Du H, He H (2018) All-carbon-electrode-based endurable flexible perovskite solar cells. Adv Funct Mater. https://doi.org/10.1002/adfm.201706777
15. Liu T, Mai X, Chen H, Ren J, Liu Z, Li Y, Gao L, Wang N, Zhang JX, He H, Guo Z (2018) Carbon nanotube aerogel-CoS2 hybrid catalytic counter electrodes for enhanced photovoltaic performance dye-sensitized solar cells. Nanoscale 10:4194–4201
16. Luo Q, Ma H, Hao F, Hou Q, Ren J, Wu L, Yao Z, Zhou Y, Wang N, Jiang K, Lin H (2017) Carbon nanotube based inverted flexible perovskite solar cells with all-inorganic charge contacts. Adv Funct Mater. https://doi.org/10.1002/adfm.201703068
17. Sun K, Fan R, Zhang Z, Shi Z, Xie P, Wang Z, Fan G, Wang N, Liu C, Li T, Guo Z (2018) An overview of metamaterials and their achievements in wireless power transfer. J Mater Chem C. https://doi.org/10.1039/C7TC03384B
18. Guo Y, Xu G, Yang X, Ruan K, Ma T, Zhang Q, Gu J, Wu Y, Liu H, Guo Z (2018) Significantly enhanced and precisely modeled thermal conductivity in polyimide nanocomposites by chemically modified graphene via in-situ polymerization and electrospinning-hot press technology. J Mater Chem C. https://doi.org/10.1039/C8TC00452H
19. Abdullah H, Lye SY, Mahalingam S, Asshari I, Yuliarto B, Manap A (2018) Gamma radiation induced nickel oxide/reduced graphene oxide nanoflowers for improved dye-sensitized solar cells. J Mater Sci Mater Electron 29:9643–9651
20. Huang J, Cao Y, Shao Q, Peng X, Guo Z (2017) Magnetic nanocarbon adsorbents with enhanced hexavalent chromium removal: morphology dependence of fibrillar vs particulate structures. Ind Eng Chem Res 56:10689–10701
21. Lin C, Hu L, Cheng C, Sun K, Guo X, Shao Q, Li J, Wang N, Guo Z (2018) Nano-$TiNb_2O_7$/carbon nanotubes composite anode for enhanced lithium-ion storage. Electrochim Acta 260:65–72
22. Ran F, Yang X, Shao L (2018) Recent progress in carbon-based nanoarchitectures for advanced supercapacitors. Advanced Composites and Hybrid Materials 1:32–55
23. Nam JG, Park YJ, Kim BS, Lee JS (2010) Enhancement of the efficiency of dye-sensitized solar cell by utilizing carbon nanotube counter electrode. Scr Mater 62:148–150
24. Kongkanand A, Domínguez M, Kamat PV (2007) Single wall carbon nanotube scaffolds for photoelectrochemical solar cells. Capture and transport of photogenerated electrons. Nano Lett 7:676–680
25. Jang SR, Vittal R, Kim KJ (2004) Incorporation of functionalized single-wall carbon nanotubes in dye-sensitized TiO_2 solar cells. Langmuir 20:9807–9810
26. Mahalingam S, Abdullah H, Shaari S, Muchtar A (2016) Improved catalytic activity of Pt/rGO counter electrode in In_2O_3-based DSSC. Ionics 22:2487–2497
27. Lu W, Liu Q, Sun Z, He J, Ezeolu C, Fang J (2008) Super crystal structures of octahedral C-In_2O_3 nanocrystals. J Am Chem Soc 130:6983–6991
28. Gan J, Lu X, Wu J, Xie S, Zhai T, Yu M, Zhang Z, Mao Y, Wang SCI, Shen Y, Tong Y (2013) Oxygen vacancies promoting photoelectrochemical performance of In_2O_3 nanocubes. Sci Rep 3:1021
29. Berki P, Nemeth Z, Reti B, Berkesi O, Magrez A, Aroutiounian V, Forro L, Hernadi K (2013) Preparation and characterization of multiwalled carbon nanotube/In_2O_3 composites. Carbon 60:266–272
30. Sönmezoğlu S, Çankaya G, Serin N (2012) Influence of annealing temperature on structural, morphological and optical properties of nanostructured TiO_2 thin films. Mater Technol 27:251–256
31. Mahalingam S, Abdullah H, Ashaari I, Shaari S, Muchtar A (2016) Influence of heat treatment process in In_2O_3-MWCNTs as photoanode in DSSCs. Ionics 22:711–719
32. Kao MC, Chen HZ, Young SL, Kung CY, Lin CC (2009) The effects of the thickness of TiO_2 films on the performance of dye-sensitized solar cells. Thin Solid Films 517:5096–5099
33. Hamadanian M, Gravand A, Farangi M, Jabbari V (2011) The effect of the thickness of nanoporous TiO_2 film on the nanocrystalline dye-sensitized solar cell, in: 5th symposium on advances in science and technology, Mashad, Iran, 12–17 May 2011
34. Lu L, Li R, Fan K, Peng T (2010) Effects of annealing conditions on the photoelectrochemical properties of dye-sensitized solar cells made with ZnO nanoparticles. Sol Energy 84:844–853
35. Huang Y, Li D, Feng J, Li G, Zhang Q (2010) Transparent conductive tungsten-doped tin oxide thin films synthesized by sol-gel technique on quartz glass substrates. J Sol-Gel Sci Technol 54:276–281
36. Jamal EMA, Sakthi Kumar D, Anantharaman MR (2011) On structural, optical and dielectric properties of zinc aluminate nanoparticles. Bull Mater Sci 34:251–259

37. Bahr JL, Yang J, Kosynkin DV, Bronikowski MJ, Smalley RE, Tour JM (2001) Functionalization of carbon nanotubes by electrochemical reduction of aryl diazonium salts: a bucky paper electrode. J Am Chem Soc 123:6536–6542
38. Sinani VA, Gheith MK, Yaroslavov AA, Rakhnyanskaya AA, Sun K, Mamedov AA, Wicksted JP, Kotov NA (2005) Aqueous dispersions of single-wall and multiwall carbon nanotubes with designed amphiphilic polycations. J Am Chem Soc 127:3463–3472
39. Baxter JB, Ayedil ES (2006) Dye-sensitized solar cells based on semiconductor morphologies with ZnO nanowires. Sol Energy Mater Sol Cells 90:607–622
40. Hara K, Zhao ZG, Cui Y, Miyauchi M, Miyashita M, Mori S (2011) Nanocrystalline electrodes based on nanoporous-walled WO_3 nanotubes for organic-dye-sensitized solar cells. Langmuir 27:12730–12736
41. Sariket D, Shyamal S, Hajra P, Mandal H, Bera A, Maity A, Bhattacharya C (2018) Improvement of photocatalytic activity of surfactant modified In_2O_3 towards environmental remediation. New J Chem 42:2467–2475
42. Bisquert J (2002) Theory of the impedance of electron diffusion and recombination in a thin layer. J Phys Chem B 106:325–333
43. Ariyanto NP, Abdullah H, Syarif J, Yuliarto B, Shaari S (2010) Fabrication of zinc oxide-based dye-sensitized solar cell by chemical bath deposition. Funct Mater Lett 3:303–307
44. Zhang B, Zhang NN, Chen JF, Hou Y, Yang S, Guo JW, Yang XH, Zhong JH, Wang HF, Hu P, Zhao HJ (2013) Turning indium oxide into a superior electrocatalyst: deterministic heteroatoms. Sci Rep 3:3109
45. Nalwa HS (1996) Encyclopedia of nanoscience and nanotechnology. American Scientific, California
46. Hara K, Horiguchi T, Kinoshita T, Sayama K, Sugihara H, Arakawa H (2000) Highly efficient photon-to-electron conversion with mercurochrome-sensitized nanoporous oxide semiconductor solar cells. Sol Energy Mater Sol Cells 64:115–134
47. Omar A, Abdullah H, Yarmo MA, Shaari S, Taha MR (2013) Morphological and electron transport studies in ZnO dye-sensitized solar cells incorporating multi-and single-walled carbon nanotubes. J Phys D Appl Phys 46:165503